J Computer-Aided Mater Des (2007) 14:177–200
DOI 10.1007/s10820-006-9031-z

Computer-aided design of transformation toughened blast resistant naval hull steels: Part I

A. Saha · G. B. Olson

Received: 3 June 2006 / Accepted: 1 September 2006 / Published online: 25 January 2007

Abstract A systematic approach to computer-aided materials design has formulated a new class of ultratough, weldable secondary hardened plate steels combining new levels of strength and toughness while meeting processability requirements. A theoretical design concept integrated the mechanism of precipitated nickel-stabilized dispersed austenite for transformation toughening in an alloy strengthened by combined precipitation of M_2C carbides and BCC copper both at an optimal ~3 nm particle size for efficient strengthening. This concept was adapted to plate steel design by employing a mixed bainitic/martensitic matrix microstructure produced by air-cooling after solution-treatment and constraining the composition to low carbon content for weldability. With optimized levels of copper and M_2C carbide formers based on a quantitative strength model, a required alloy nickel content of 6.5 wt% was predicted for optimal austenite stability for transformation toughening at the desired strength level of 160 ksi (1,100 MPa) yield strength. A relatively high Cu level of 3.65 wt% was employed to allow a carbon limit of 0.05 wt% for good weldability, without causing excessive solidification microsegregation.

Keywords Yield strength · Fracture toughness · Weldability · Copper strengthening · Hardness · Transformation toughening · Austenite · Stability · Dispersion · Precipitation

A. Saha (✉) · G. B. Olson
Department of Materials Science and Engineering, Robert R. McCormick School of Engineering and Applied Science, Northwestern University, 2220 Campus Drive, Evanston, IL 60208, USA
e-mail: arup.saha@intel.com

Present Address:
A. Saha
Intel Corporation, 2501 NW 229th Avenue, RA3-355, Hillsboro, OR 97124, USA

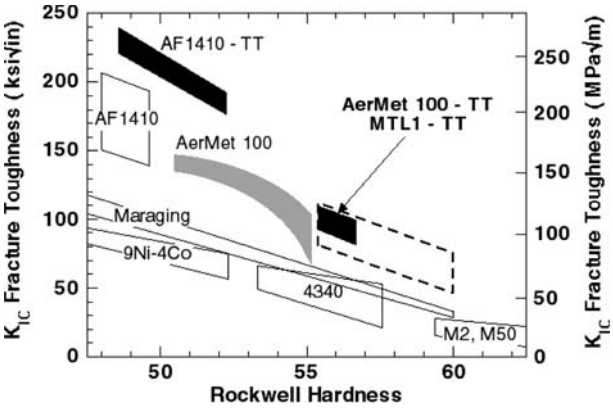

Fig. 1 K_{IC} toughness versus R_C hardness cross-plot for ultra-high strength martensitic steels [1]

1 Introduction

With scientific advances in the past century, the property-driven view of structure and processing for the creation of value has motivated the development of a systematic strategy in computer-aided design of materials [1,2]. The approach combines materials science, quantum physics and continuum mechanics in the integration of process/structure/property/performance relations for predictive design of high performance steels as multilevel dynamic structures. Throughout the history of materials development, there has been an ever-increasing need for stronger, tougher, more fracture resistant and easily weldable plate steels for structural applications at minimal cost. Unfortunately, however, any increase in strength is rarely achieved without concomitant decreases in toughness and ductility, which limits the utility of most ultra-high-strength steels. The best combinations of strength and toughness have usually been obtained from martensitic microstructures as shown in Fig. 1. High strength bainitic steels have not been as successful in practice because of the coarse cementite particles in bainite that are detrimental to toughness. The primary benefit motivating the research of air-hardened steels containing bainite/martensite mixtures is the ease of processing, which finally leads to a product with good performance at a relatively lower cost. There is then the possibility of improving the strength and toughness simultaneously using fine-grained bainitic ferrite plates and enhancing the toughness by transformation toughening effects. Further improvements of strength can be achieved with co-precipitation of alloy carbides and BCC copper for easily weldable low-carbon steels [3], where alloy carbide precipitation dissolves the deleterious cementite.

It is now well established that the interaction of deformation-induced martensitic transformation of dispersed austenite with fracture-controlling processes such as microvoid induced shear localization results in substantial improvements in fracture toughness called Dispersed Phase Transformation Toughening (DPTT). This is the toughening mechanism modeled and investigated in this work. Transformation toughening is attributed to modification of the constitutive behavior of the matrix through pressure-sensitive strain hardening associated with the transformation volume change

[4,5]. The transformation behavior and the toughening effects are controlled by the stability of the austenite dispersion. For transformation toughening at high strength levels, the required stability of the austenite dispersion is quite high and can be achieved only by size refinement and compositional enrichment of the austenite particles. The size influences the characteristic potency of nucleation sites in the particles while the composition influences the chemical driving force and interfacial friction for the martensitic transformation. The size refinement and the compositional enrichment of the austenite can be controlled with heat treatments such as multistep tempering [6].

Combining new levels of strength and toughness while meeting processability requirements, the design addressed here will focus on a new class of ultratough, weldable secondary hardened bainitic/martensitic plate steels for blast resistant naval hull applications.

2 Design objectives

Looking ahead to the projected naval hull material requirements in the year 2020, the primary design objectives motivating this research are the achievement of extreme impact fracture toughness ($C_v > 85$ ft-lbs or 115 J corresponding to fracture toughness, $K_{Id} > 200$ ksi $in^{1/2}$ or 220 MPa $m^{1/2}$ and $K_{Ic} > 250$ ksi $in^{1/2}$ or 275 MPa $m^{1/2}$) at high strength levels of 150–180 ksi (1,030–1,240 MPa) yield strength in weldable, formable plate steels with high resistance to hydrogen stress corrosion cracking ($K_{ISCC}/K_{IC} > 0.5$) [18,19]. Because of difficulties in measurement of K_{Id} and K_{Ic} fracture toughness at such extreme levels, toughness of prototypes will be assessed by Charpy impact energy (C_V) absorption measurements; details of the $K_{Ic} - C_V$ and $K_{Id} - C_V$ toughness correlation will be discussed later. The primary design goals are marked by the star in the cross-plot of K_{Ic} fracture toughness and yield strength illustrated in Fig. 2. This design aims to substantially expand the envelope marked as "steels" to the top right corner of the plot.

3 Design approach

Based on Cyril Smith's [8] modern systems view of materials structure as "universal multilevel structure with strong interactions among different levels…" this materials design approach breaks down the complex nature of the structural hierarchy to better understand the structure and property relations underlying the technological and economic value of materials. Our approach follows the framework of systems engineering as outlined by Jenkins [9]. Once the final goal has been set, the structure is described as subsystems with graphical representation of the interactions through a system flow block diagram. The flow block diagram represents the key microstructural subsystems, links them to the properties they control and then to the stages of processing that govern their dynamic evolution. Because of the complex nature of materials, it should be realized that the interaction between the subsystems is as important as the subsystems themselves. The systems analysis is then applied to identify and prioritize the key structure–property and processing–structure relations. Figure 3 describes the system structure adopted here to design a steel with the specified strength and

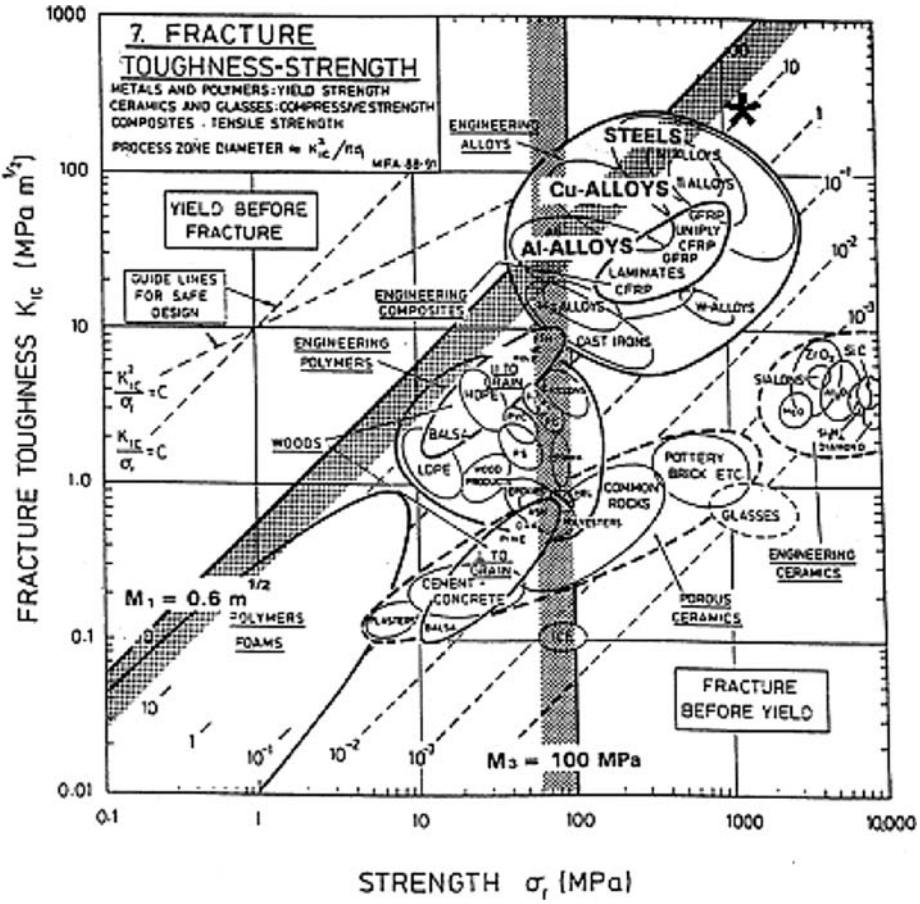

Fig. 2 K_{IC} toughness versus σ yield strength cross-plot for different classes of materials [7]

toughness levels while meeting composition and processing constraints for weldability and hydrogen resistance.

Our system-level design integration follows a multiobjective "satisficing" approach [9], with aspects of single-objective optimization applied at the subsystem level based on previously established quantitative structure/property relations for strength and toughness. Quantitative design integration follows a parametric approach, expressing microstructural subsystem requirements in terms of thermodynamic parameters and employing computational thermodynamics to iteratively solve for a self-consistent alloy composition balancing the conflicting subsystem requirements. Alloy processability is addressed as constraints on overall composition and transformation temperatures.

With toughness being a major priority for this design, the matrix was chosen as a secondary hardened bainite/martensite mixture, in which cementite particles should be eliminated by alloy carbide precipitation in "Stage IV" tempering, as they are detrimental to the toughness of the steel. In addition, an optimum-stability austenite dispersion in the bainitic/martensitic matrix can also help in increasing the

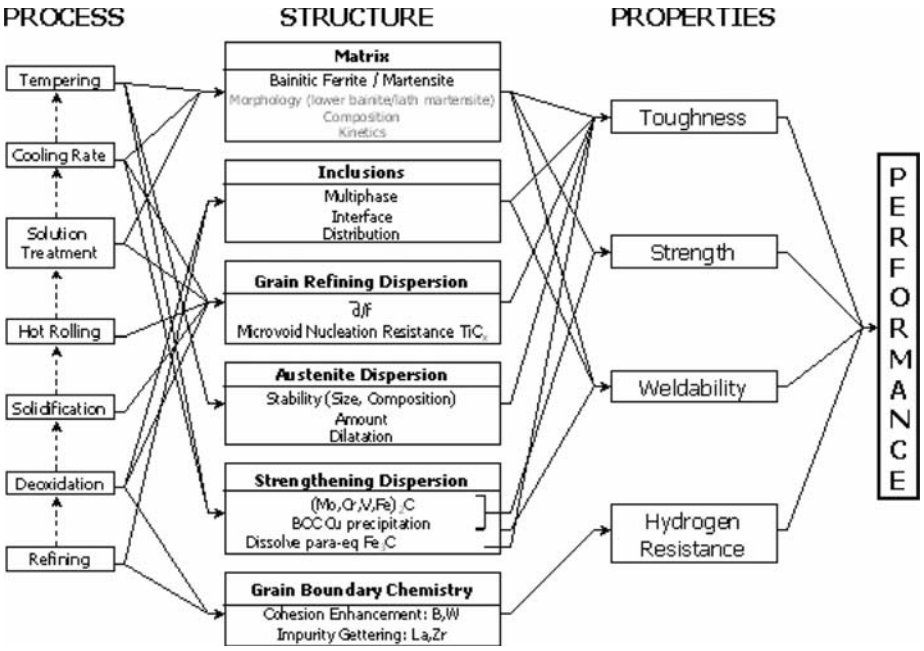

Fig. 3 Material system chart for design of blast resistant naval hull steels

toughness of the steel. Our previous studies [10,11] have demonstrated exceptionally large fracture toughness values in high-strength precipitation-hardened metastable austenitic steels. This remarkable increase in the fracture toughness is attributable to the process of transformation toughening which will be discussed in greater detail later. Recent studies [12] have also shown that selection of fine Ti(C, N) as a grain refining dispersion contributes to increasing the fracture resistance by delaying the coalescence of microvoids among the primary voids. Studies [13] have also suggested that the resistance to primary void formation and coalescence is proportional to inclusion spacing. It is thus desirable to reduce the volume fraction of primary inclusions or coarsen inclusions for a given volume fraction. This can be achieved by clean melt practices and tight composition control. However, engineering design fracture toughness parameters like K_{Ic} and K_{Id} are difficult and expensive to measure. Thus for preliminary design analyses, small-scale inexpensive fracture measurements like Charpy V-notch impact energy (C_{V}) values can be used to estimate K_{Ic} and K_{Id}. Studies of fracture toughness dependence on loading rate measured over a temperature range [14] have shown that K_{Ic} fracture toughness values under static and intermediate loading are about 20% higher than the K_{Id} measured under impact loading. While it is known that K_{Ic} and C_{V} cannot be universally correlated [15], Barsom and Rolfe [14] have established an approximate relation between K_{Ic} and C_{V} test results for conventionally grain-refined steels:

$$K_{\mathrm{IC}}^2 = AC_{\mathrm{V}} \tag{1}$$

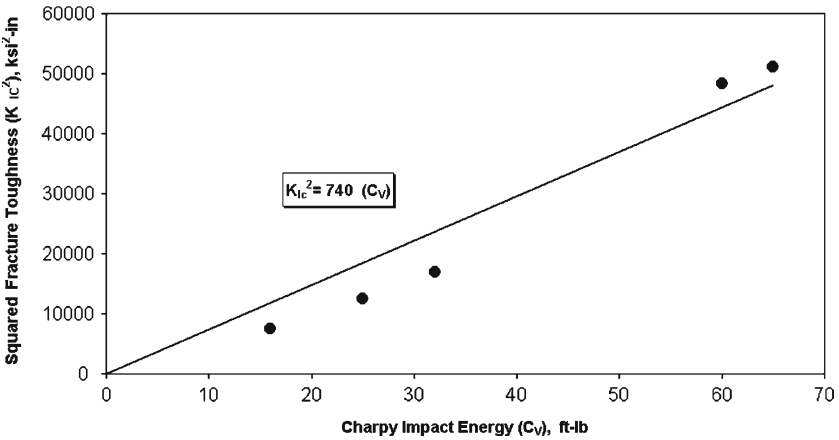

Fig. 4 Correlation between K_{Ic} and C_V test results [14] for high Ni steels

where A is a constant of proportionality. Fitting Eq. 1 to results from high Ni steels shown in Fig. 4, an empirical correlation can be established for the class of steels explored in this study.

According to these relationships, the C_V impact toughness objective of 85 ft-lbs is equivalent to the K_{Ic} fracture toughness of 250 ksi $in^{1/2}$(275 MPa $m^{1/2}$) represented in Fig. 2, corresponding to a dynamic K_{Id} of 200 ksi $in^{1/2}$ (220 MPa $m^{1/2}$).

A fine carbide dispersion must be obtained in order to achieve the desired strength level. Coherent M_2C carbides have been used in secondary hardened steels that are currently in use [16]. Previous work [17] to optimize the carbide particle size for strength has shown that 3 nm carbide precipitates corresponding to the transition from particle shear to Orowan bypass provide maximum strength. Thermodynamics and kinetics of carbide precipitation have to be controlled to obtain such a fine M_2C carbide dispersion. The driving force for M_2C nucleation should be maximized by proper control of the amount and ratio of carbide formers in the alloy to refine the M_2C particle size. Sufficient M_2C precipitation must be achieved to dissolve cementite in order to attain the desired toughness levels because coarse cementite particles are extremely deleterious as microvoid nucleation sites. Tempering times should also be minimized to prevent impurity segregation at grain boundaries.

Even if we maintain low alloy carbon levels, higher alloying content tends to reduce weldability by increasing hardenability. For any structural material, the heat-affected zone (HAZ) adjacent to the welded joints are considered to be the weakest links. Weldability of steels is controlled by both the matrix and the strengthening dispersion structures. As a rule of thumb, for adequate weldability of the steel C content of the alloy should be kept below 0.15 wt%. This in turn limits the C available for M_2C strengthening. For the bainitic matrix, if we modify the hardenability of the steel, we can obtain bainite with a much lower cooling rate. This becomes a trade-off since weldability can deteriorate as the hardenability increases.

Ultra-high strength steels are prone to a decrease of fracture toughness in aqueous environments due to hydrogen assisted cracking. This reduction of toughness is caused by intergranular brittle fracture associated with impurity segregation to grain boundaries, which may reduce toughness of the steel by as much as 80% in a

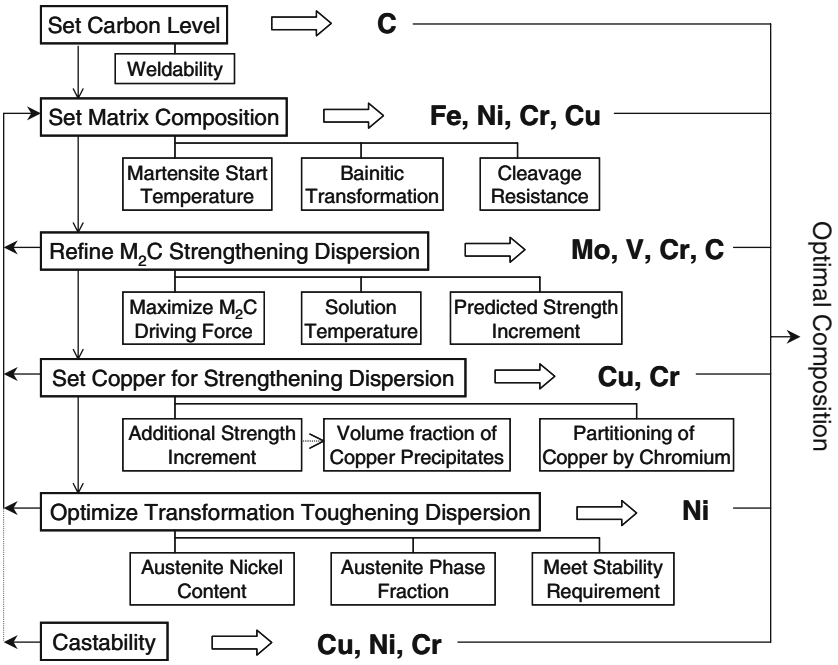

Fig. 5 Schematic of the design procedure

corrosive environment. The common impurities in steel are P and S, both of which are embrittlers since they have lower free energy on a surface than at a grain boundary. The most effective way of reducing them is by cleaner processing techniques or impurity gettering. Impurity gettering can tie up P and S as stable compounds formed during solidification. La and Zr have been found to be effective impurity gettering elements. Another approach to minimize impurity effects is by design of grain boundary chemistry. Segregating elements like W and Re [18,19] preferentially on the grain boundaries that enhance grain boundary cohesion is beneficial to the stress corrosion cracking resistance. Small amounts of dissolved B also help in grain boundary cohesion. As denoted at the lowest level of the system chart of Fig. 3, these issues are addressed by trace element composition constraints set at the earliest stage of material processing.

Based on the above considerations for the property → structure → processing relationships of the overall design system, Fig. 5 presents a schematic process flow of the iterative design integration procedure employed in this work to determine a theoretical design composition. Each of the steps of this process will next be discussed in turn.

3.1 Strength design

An efficient approach to strengthen the steel while limiting carbon content for weldability is co-precipitating M_2C carbides and BCC copper. By trading off the interaction between particle size and the phase fraction of the precipitates, the goal of high-strength can be achieved.

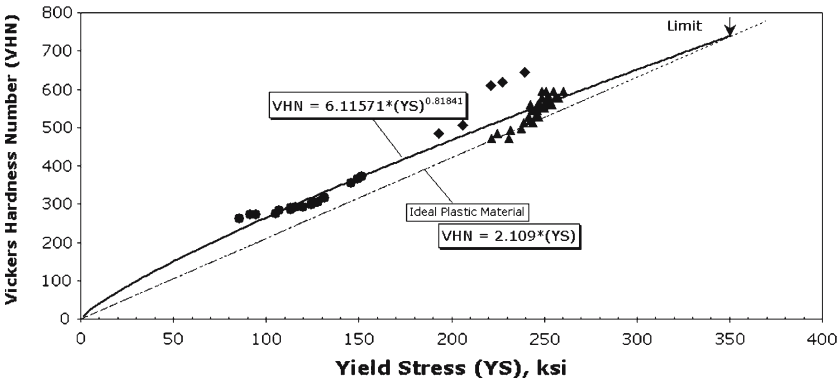

Fig. 6 Power-law relationship relating hardness of related steels to yield stress from experimental data from Foley [21] (circles), Kuehmann [22] (triangles) and Spaulding [23] (diamonds) shown in comparison to straight-line relationship for ideal plastic material

3.1.1 Quantitative strengthening contributions

As highlighted by the system design chart (Fig. 3), the strength of the alloy will be designed by using quantitative strengthening models to predict its dependence on the structure of the steel. To achieve a goal of 160 ksi (1,100 MPa) yield strength, quantitative models will be employed to relate the contribution from dispersions of M_2C carbide precipitates [17] and BCC copper precipitates [20] in secondary hardened steels. The levels of M_2C carbide formers and copper will be selected based on the strength contribution from each of these substructures. In this work, assessment of the yield strength of the material has been made directly from the hardness data because of the ease and convenience in measurement of the latter. Hardness of a material is a direct manifestation of its resistance to plastic flow, monotonically relating to yield stress. An empirical relationship has been developed between hardness and yield stress based on experimental data from previous research on related steels: HSLA100 data from Foley [21], AerMet100 data from Kuehmann [22] and SRG C2 experimental gear steel data from Spaulding [23]. The best-fit curve in a log–log plot of hardness versus yield stress has been used to determine the relationship incorporating strain hardening effects. Figure 6 presents the experimentally measured hardness—yield stress data from the previous research superimposed with the best-fit power-law relationship and the theoretical straight-line relation describing the same for an ideal plastic material [24]. The higher hardness of the empirical power-law relationship relative to the ideal-plastic case represents the effect of strain hardening, which is more pronounced at lower strength levels. The point at which the two curves meet represents the prediction limit of the relationship.

Thus, the hardness estimate for the target yield strength of 160 ksi (1,100 MPa) from the power-law relationship is 389 VHN. The relationship obtained is:

$$\mathrm{VHN} = 6.116\mathrm{YS}^{0.8184} \tag{2}$$

where VHN (Vickers Hardness Number) is in kg/mm^2 and YS (Yield Strength) is in ksi.

The first step in the design involved setting the carbon content of the alloy to ensure good weldability. Figure 7 presents the Graville diagram summarizing effects of overall

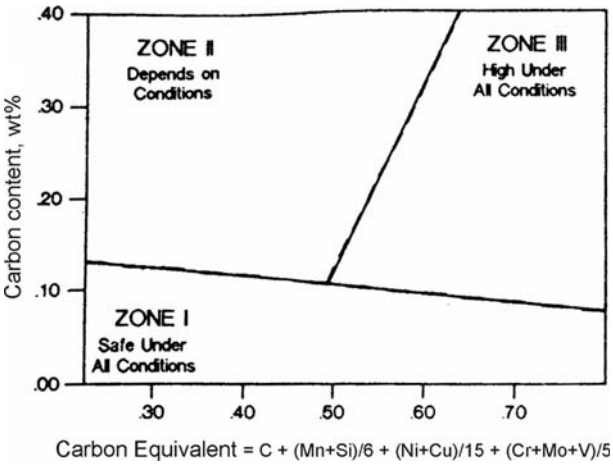

Fig. 7 Graville diagram for determining susceptibility to HAZ cracking in plate steels [25]

carbon content and alloy carbon equivalent. This shows that at 0.05 wt% C, the steel is not susceptible to hydrogen—induced cold cracking in the heat affected zone (HAZ) of weldments. Consistent with the carbon level in current Navy HSLA100 steel, the lower limit C content of 0.05 wt% C was set for the alloy, thus allowing relatively high carbon equivalent levels of alloy content.

Based on the effect of M_2C carbide precipitates in the Orowon bypass regime, Wise [17] developed a quantitative strength model to predict the strengthening achieved for a given carbon level. The predictions assume that a given carbon content of the alloy is precipitated to the full equilibrium carbide volume fraction and considers carbides of fixed particle diameter. Based on the predicted change in hardness-carbon content (wt%) plot shown in Fig. 8, at a C level of 0.05 wt% the hardness increment due to M_2C carbide precipitation is estimated to be 175 VHN provided a sufficient driving force is maintained to achieve the particle size range of ~4–5 nm in Fig. 8. The base strength of a lath martensitic substructure was estimated as 63 VHN by Wise [17]. The additional strength increment of 151 VHN to achieve the strength goal of 389 VHN must then be attained through BCC copper precipitation strengthening, described later. The effect of solid solution strengthening is assumed to be negligible for steels having low carbon and low hardenability. Thus, the total strength of the alloy has been modeled by superimposing three contributions. The strength is described by the effects of M_2C carbide precipitates, τ_{M2C}; BCC copper precipitates, τ_{Cu} and matrix martensitic structure, $\tau_{\alpha'}$.

$$\tau = \Delta\tau_{M2C} + \Delta\tau_{Cu} + \Delta\tau_{\alpha'} \equiv 389\text{VHN} \tag{3}$$

The contributions of the individual mechanisms to achieve the strength goal equivalent to 389 VHN are graphically presented in Fig. 9.

3.1.2 M_2C carbide strengthening

For the high-strength design, we want to ensure that all of the carbon is taken up by the M_2C carbide formers (Cr, Mo and V) in order to dissolve the cementite in the matrix.

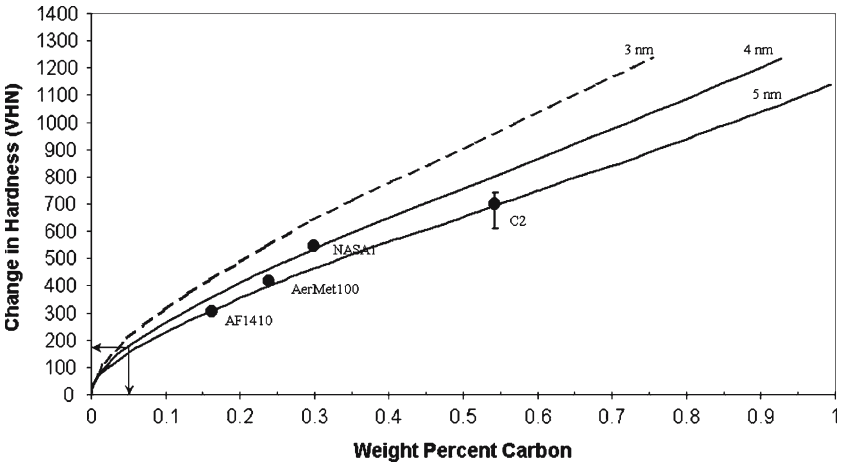

Fig. 8 Change in hardness as a function of alloy carbon content for M_2C carbide strengthening contribution [17]. The arrows represent hardness increment of 175 VHN is achieved at C level of 0.05 wt% set for the alloy. Experimental results of other secondary hardening steels are shown

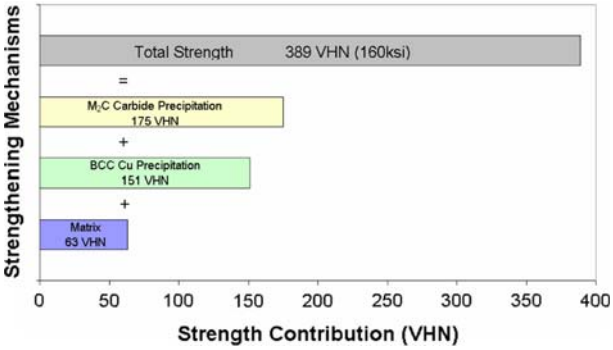

Fig. 9 Graphical representation for contributions of the individual mechanisms to achieve the strength goal equivalent to 389 VHN

Cementite negatively affects strength and toughness. Therefore, we want the sum of the atomic concentrations of Cr, Mo and V to be at least double the concentration of C for the M_2C stoichiometry.

A series of calculations were performed in order to design a steel that meets the strength requirements. Preliminary compositions were set using the guideline (consistent with the HSLA100 alloy) that carbon content should be limited to 0.05 wt% for weldability (Fig. 7); Cu should be at least 1.5 wt% for significant strengthening [21,26], minimum Ni content should be at least half that of Cu to avoid hot shortness, and the relative amounts of carbide formers Cr, Mo and V was initially set equal in atomic percent. A feasibility study was then performed to ensure that this strengthening concept, in conjunction with our approach for toughening (described later) is thermodynamically possible, i.e. all of the phases needed for precipitation strengthening and nickel-stabilized austenite could co-exist at least in metastable equilibrium at processing temperatures. A BCC Cu-rich precipitate is necessary for Cu precipitation

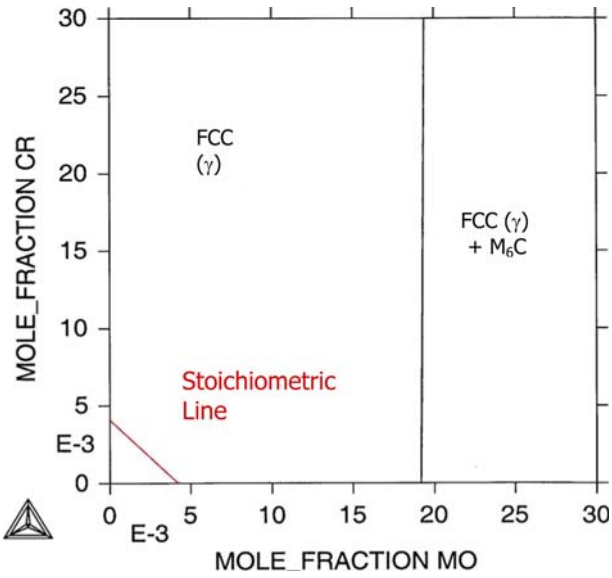

Fig. 10 Cr–Mo phase diagram section at 900°C with alloy composition in atomic %: Fe–0.234C–1.32Cu–6.21Ni–0.055V. This diagram shows the phase fields of the FCC austenite and FCC + M_6C revealing that the M_2C stoichiometric line is well within the solubility limit

strengthening, an M_2C carbide phase is necessary for carbide strengthening, and FCC austenite is critical for transformation toughening. Considering these constraints, thermodynamic feasibility of the preliminary alloy composition was verified by *Thermo-Calc*™ [27] calculations at kinetically reasonable tempering temperatures of 400–500°C using the SGTE/SSOL thermochemical database.

Before the driving forces were calculated, a Mo–Cr phase diagram section at a solution temperature of 900°C was calculated in order to determine the relative solubility of the carbide formers in the austenite phase at a reasonable solution temperature. The solubility limit should not be exceeded in order to achieve full conversion to M_2C for maximum carbide strengthening. Recalling that the M_2C stoichiometry must be maintained, the stoichiometric constraint, as well as the solubility limit, can be superimposed onto a contour plot of driving force versus Mo and Cr concentration to optimize the M_2C driving force. The Mo–Cr phase diagram section is shown in Fig. 10. It is apparent from the diagram that solubility is not a limiting factor in the region of interest, due to the relatively limited C content.

The stoichiometric constraints of the M_2C carbide dictated that the total amount of carbide formers (Cr, Mo, V) needed to balance the carbon content would be 0.468 at%. Using this constraint, initial plots were constructed of the driving force for M_2C nucleation versus at%(Mo) and at%(Cr), setting V at different levels. Figure 11 is a representative plot of driving force contours with varying at%(Mo) and at%(Cr) at a constrained composition of 0.05 at% V at 500°C. The stoichiometric constraint line has been drawn on the plot indicating the line of allowed compositions for M_2C. This study indicated that Cr has the least effect on driving force, especially at the higher contents of interest.

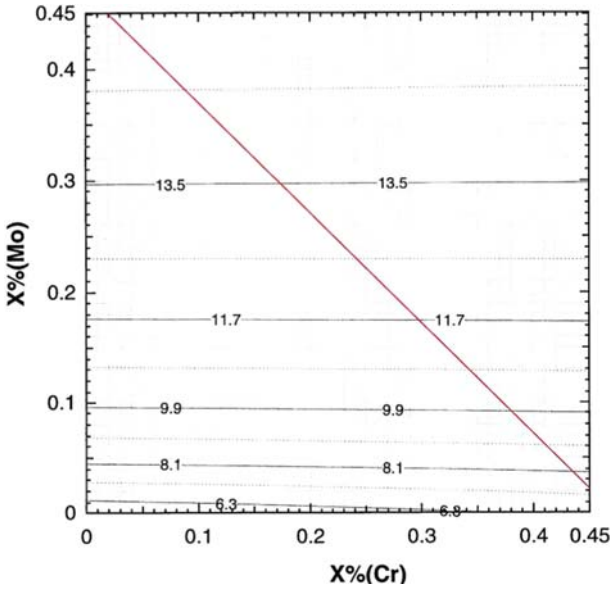

Fig. 11 Driving forces (in kJ/mole) for M_2C carbide nucleation contour plot varying at%(Mo) and at%(Cr) with superimposed M_2C stoichiometric (heavy) line at 500°C at alloy compositions at% Fe–0.234C–1.32Cu–6.21Ni–0.055V

Based on this finding, another set of driving force plots were created varying at%(Mo) and at%(V) while setting the Cr level at fixed values. Due to the very small Cr dependence, all the plots were very similar and so only a representative graph (Fig. 12) is included here at 0 at%(Cr). A similar M_2C stoichiometric line was drawn as before, constraining a maximum driving force at about 14.4 (kJ/mole). This plot revealed an almost equal effect on driving force for Mo and V, indicating that any allowed ratio of the two should give a maximum driving force value, so a series of calculations were done along the stoichiometric line (maximum driving force). We found a feasible alloy composition where all the desired phases as mentioned before co-existed, which is indicated by the point and arrow in Fig. 12. An initial feasible alloy composition in wt% was thus determined without any Cr: Fe–0.05C–1.5Cu–6.5Ni–0.6Mo–0.1V.

The V–Mo phase diagram section at a solution temperature of 900°C with the feasible alloy composition was then calculated. Again, the solubility of these carbide formers is not a limiting factor in the region of interest. This plot is shown in Fig. 13.

3.1.3 Copper precipitation strengthening

In addition to M_2C carbide strengthening, BCC copper precipitation strengthening will be modeled to control the phase fraction of the precipitates through the alloy copper content to provide the additional increment of strength (≡151 VHN). The copper precipitates that contribute to strengthening in steels have a metastable BCC structure, which are fully coherent with the matrix having an average diameter of 1–5 nm [28–35]. The strengthening mechanism has been described by the Russell–Brown model [20] based on the interaction between the matrix slip dislocation and the second phase

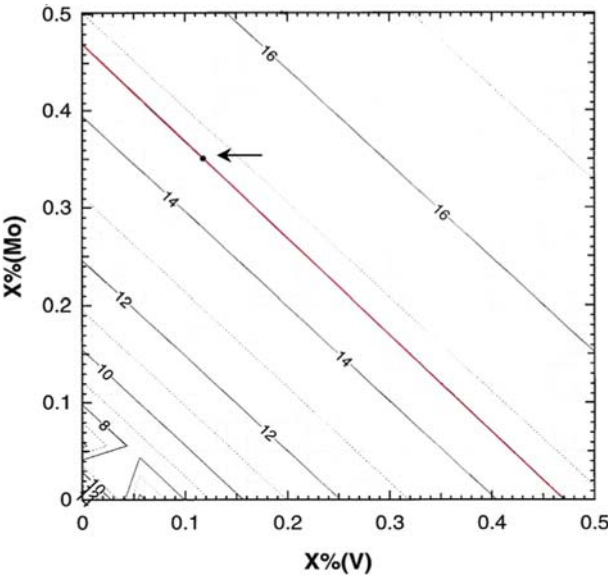

Fig. 12 Driving force (in kJ/mole) for M_2C carbide nucleation contour plot varying at%(Mo) and at%(V) with superimposed M_2C stoichiometric line at 500 °C at alloy compositions at% Fe–0.234C–1.32Cu–6.2Ni

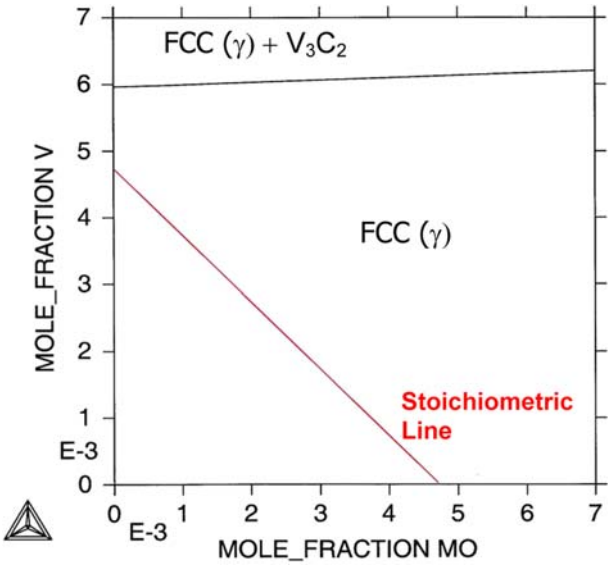

Fig. 13 Mo–V phase diagram section at 900°C with alloy composition in atomic %: Fe–0.234C–1.32Cu–6.2Ni. This diagram shows the phase fields of the FCC austenite and FCC + V_3C_2 revealing that the M_2C stoichiometric line is well within the solubility limit

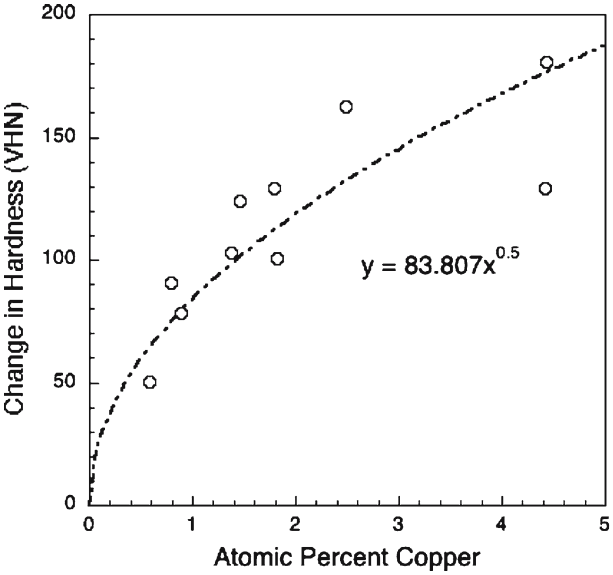

Fig. 14 Change in peak hardness as a function of alloy copper content for BCC copper strengthening contribution [20]. Experimental results of other copper strengthened steels are shown. The dotted line represents the best-fit line for one-half power law given by Eq. 5

copper-rich particle of lower shear modulus than the matrix. The shear stress has a maximum value, $\tau_{\max}$, given by Eq. 4.

$$\tau_{\max} = \frac{0.041 G b f^{1/2}}{r_0} \tag{4}$$

where, G is the matrix shear modulus, b is the burgers vector, f is the volume fraction of precipitates and r_0 is the core radius of the dislocation. The maximum strength that can be achieved (which empirically occurs at a particle diameter of 2–3 nm) is thus proportional to the square root of the volume fraction of the precipitate. Based on this volume fraction dependence of the precipitate on yield stress, the peak hardening increment from available data of copper precipitation strengthened steels [20] was plotted as shown in Fig. 14. The best-fit line described by a one-half power law defined the hardening increment dependence on the alloy content (at%) of copper.

$$\Delta\tau(\text{VHN}) = 83.807 X_{\text{Cu}}^{1/2} \tag{5}$$

giving a strengthening coefficient within a factor of ~1.2 of the Russell–Brown estimate. Based on this relationship, the hardness increment of 151 VHN can be achieved by addition of 3.25 at% Cu to the alloy composition, provided this level can be made soluble at the alloy austenizing temperature.

3.2 Transformation toughening design

For design of tough steels for such high strength levels (160 ksi or 1,100 MPa YS) we need to develop a fully secondary hardened microstructure with high stability austenite produced by precipitation. At high strength levels we need high stability of

precipitated austenite since the mechanical driving force for transformation is very high. This design seeks to improve the toughness of higher strength steels by utilizing the beneficial properties of Ni-stabilized precipitated austenite. This form of austenite can precipitate during annealing or tempering at elevated temperatures above about 470°C. The fact that this dispersed austenite forms by precipitation is significant because it allows greater overall control of the amount and stability of the austenite. Further processing and treatments can be used in the form of multistep tempering to first nucleate particles in a fine form at a higher tempering temperature and then complete Ni enrichment during completion of precipitation strengthening (cementite conversion to M_2C) at a lower final tempering temperature [4,6].

Shear localization by microvoid nucleation is known to be the most dominant fracture mode in high toughness steels. Studies [36] have shown that fine particle dispersions with adherent interfaces are most useful for controlling microvoid nucleation. The most promising microstructure modification is achieved by nucleating an optimal stability austenite dispersion, which increases toughness by suppressing microvoid nucleation to higher strain levels. Thus, emphasis will be put on the design of intralath dispersions, as the greater stability associated with their finer size makes them the primary toughening form of austenite precipitates.

The austenite dispersion must have sufficient stability and proper formation kinetics to ensure maximum toughening enhancement. Other factors controlling the stability of austenite are particle size and stress state sensitivity, the latter being related to the transformational volume change. The Olson–Cohen classical heterogeneous martensitic nucleation model can be applied to describe dispersed austenite stability for transformation toughening [4]. Stability of an austenite precipitate is defined by chemical and mechanical driving force terms. At the M_s^σ temperature (where transformation occurs at yield stress) for the crack-tip stress state, the total driving force equals the critical driving force for martensite nucleation, as represented by Eq. 6.

$$\Delta G^{\mathrm{ch}} + \sigma_y \left.\frac{\mathrm{d}\Delta G^\sigma}{\mathrm{d}\sigma}\right|_{\mathrm{cracktip}} = -\left[\frac{2\gamma}{nd} + G_0 + W_{\mathrm{f}}\right] \tag{6}$$

Rearranging the terms and substituting a dependence of defect potency on particle volume V_{p} [37], we can define a convenient stability parameter:

$$\Delta G^{\mathrm{ch}} + W_{\mathrm{f}} + \frac{K}{\ln(V_{\mathrm{p}})} = -\left[\sigma_{\mathrm{y}} \left.\frac{\mathrm{d}\Delta G^\sigma}{\mathrm{d}\sigma}\right|_{\mathrm{cracktip}} + G_0\right] \tag{7}$$

ΔG^{ch} is the transformation chemical free energy change and W_{f} is the athermal frictional work term ΔG^{ch} is temperature and composition dependent while W_{f} is only composition dependent. W_{f} will vary with tempering temperature due to the change in austenite composition. σ_{y} is the yield stress of the material, ΔG^σ is set by the stress state and G_0 is a fixed stored energy term. K is a proportionality constant, γ is the nucleus specific interfacial energy and d is the crystal interplanar spacing.

The austenite stability for a given set of conditions or service temperature for a given dispersion can be assessed by the parameter given by the left-hand side of Eq. 7. If we assume an austenite particle size equivalent to that achieved in previous studies of AF1410 and AerMet100 steels, our austenite stability parameter becomes the sum of the chemical driving force for transformation of FCC austenite to BCC martensite at room temperature (300 K) and the frictional work term for martensitic interfacial motion: $\Delta G_{\mathrm{ch}} + W_{\mathrm{f}}$. *ThermoCalc*™ can be used with an appropriate thermochemical

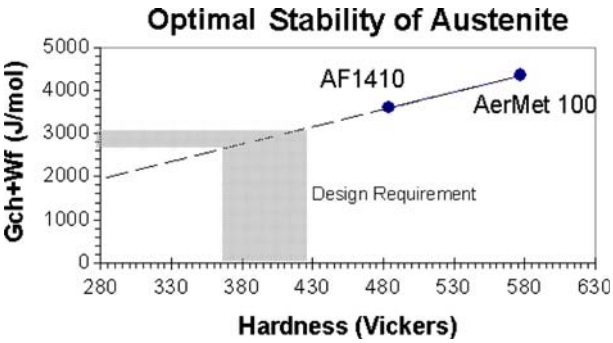

Fig. 15 Optimal room temperature (300 K) austenite stability plotted as a function of Vickers Hardness Number (VHN). The shaded region shows our range of interest for austenite stability corresponding to a yield strength requirement of 150–180 ksi (1030–1240 MPa) after extrapolation of data from previous alloys, AF1410 and AerMet100

Table 1 Target chemical driving force (ΔG_{ch}) + frictional work (W_f) value

Alloy	Rockwell C Hardness R_c	Vickers Hardness VHN (kg/mm^2)	$\Delta G_{ch} + W_f$ J/mol
AerMet 100	54	577	4350
AF1410	48	484	3600
Design	40	389	2837

database [38] to predict the temperature and compositional dependence of the chemical energy term. Ghosh and Olson [38,39] have modeled the composition dependence of the frictional work term as a power law with an exponent of 0.5 and a fit to experimental data. Appropriate superposition laws considering relative strengths of the solutes were applied for complex systems. The model is represented in Eq. 8.

$$W_f = \sqrt{\sum_i \left(K^i X_i^{1/2}\right)} + \sqrt{\sum_j \left(K^j X_j^{1/2}\right)} + \sqrt{\sum_k \left(K^k X_k^{1/2}\right)} + K^{Co} X_{Co}^{1/2} \qquad (8)$$

where the K's represent the coefficients used to fit the solid solution strengthening data and i = C, N; j = Cr, Mn, Mo, Nb, Si, Ti, V; and k = Al, Cu, Ni, W. Equation 7 further indicates that the stability parameter is a linear function of the yield strength of the material.

Thorough studies of transformation toughening [10,11] have demonstrated that maximum toughening occurs at the M_S^σ temperature for the crack-tip stress state, thus quantifying an optimal austenite stability. The strength dependence of this optimal stability level at fixed V_P was determined from previous dispersed-phase transformation toughening optimization experiments on the AF1410 and AerMet100 steels [40]. Figure 15 gives a plot of the measured optimal stability, $\Delta G_{ch} + W_f$, at room temperature against Vickers hardness of the alloy. The required room temperature stability of the austenite dispersion projected from the hardness (or strength) requirement of the design is marked by the shaded region in the figure and quantitatively expressed in Table 1. To achieve a goal of 160 ksi (1,100 MPa) yield strength equivalent to Vickers hardness of 389 (Rc40 equivalent), the estimated value of $\Delta G_{ch} + W_f$ for the required stability is determined to be 2,837 J/mole.

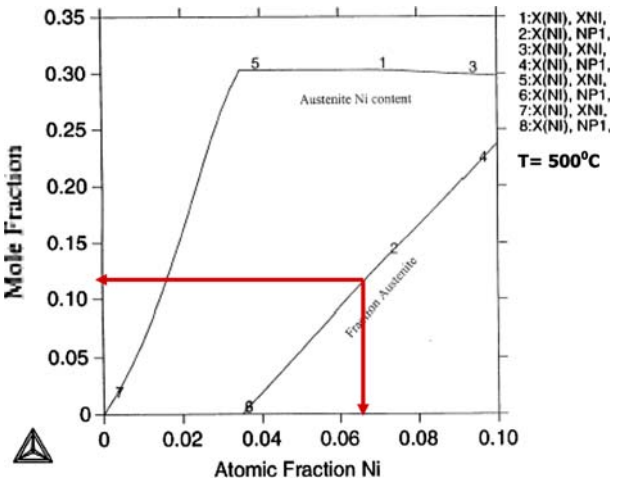

Fig. 16 Fraction of Ni in austenite and phase fraction of austenite in alloy versus mole fraction of Ni at 500°C with alloy composition in weight%: Fe–0.05C–3.65Cu–1.85Cr–0.6Mo–0.1V

The design of transformation-toughened austenite has been calibrated against this stability parameter to determine the optimal level of austenite-stabilizing nickel in the alloy. Plots of both the phase fraction of austenite and nickel content in the austenite phase versus alloy atomic fraction Ni were computed. Figure 16 was calculated at an estimated final tempering temperature of 500°C for substitutional diffusion and revealed that a minimum of 3.5 at% Ni is required to get austenite and a maximum content of nickel in the austenite of about 0.30 could be obtained. It also showed that at the 6.25 at% Ni composition from initial feasibility studies, about a 0.10 phase fraction of austenite would be formed as shown by the arrows. This compares well to the phase fraction of austenite employed in previous transformation toughened steels. We thus set the alloy Ni level to 6.25 at%, which also saturates the austenite Ni content to 30 at%.

After conducting the feasibility study mentioned earlier and verifying that the corresponding austenite stability was within the design limits given in Fig. 15, a thermodynamically viable alloy composition was found using 6.25 at% Ni. This Ni level was deemed acceptable as it fell well within the nickel content guidelines, while being low enough to limit the material cost.

3.3 Composition integration

The overall composition was next optimized so that all of the phases necessary for strengthening and toughening are simultaneously present. The full sequence of iterative calculations followed the flow chart of Fig. 5. Since the maximum M_2C driving force at fixed total solute is obtained with no chromium, equilibrium phase calculations were done for the initial feasible composition. For this initial composition, it was found that the copper added for precipitation strengthening went instead into the austenite phase. It was found that Cr partitions Cu out of austenite and into the BCC precipitate phase effectively at 2 at% and above, and the Cr content was thus set to this minimum value. The iterative calculation sequence of Fig. 5 then yielded a

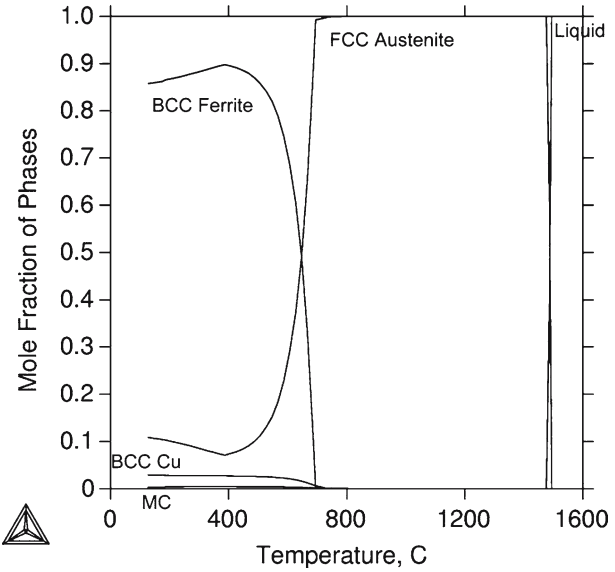

Fig. 17 Equilibrium mole fraction of phases in the alloy as a function of temperature, showing that the alloy is solution treatable at 900 °C

self-consistent alloy composition meeting all phase relation requirements. The composition was then further evaluated from the viewpoint of processability requirements.

4 Processing considerations

4.1 Solution treatment temperature and allotropic transformations

A solution treatment temperature of 900°C was chosen based on previous optimization studies [22,41] on grain size dependence of hardness and toughness based on 1-h solution treated samples in secondary hardened steels. With the increased levels of Cu and Cr it was confirmed that the alloy was solution treatable at 900°C as shown by the *ThermoCalc*™ phase fraction plot in Fig. 17.

For this alloy composition, our martensite and bainite kinetic models predict an M_S temperature of 298°C and a bainite start (B_S) temperature of 336°C. These should be sufficiently high to allow formation of bainite/martensite mixtures with air-cooling.

4.2 Scheil simulation for microsegregation behavior

Solidification of alloys generally occurs with segregation, which can have a strong effect on the alloy's final properties. Thus, it is important to model segregation to assess the processability of the designed alloy. This investigation uses thermodynamic modeling to predict microsegregation of the as-cast material. Macrosegregation effects can also be addressed by modeling liquid buoyancy associated with the microsegregation amplitude but are not addressed in this assessment.

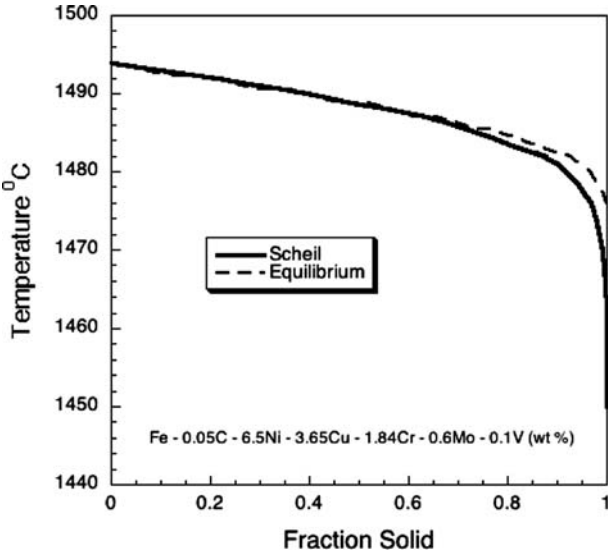

Fig. 18 Scheil simulation for evolution of the fraction solid with cooling for designed alloy Fe–0.05C–6.5Ni–3.65Cu–1.84Cr–0.6Mo–0.1V (wt%) in comparison with equilibrium solidification

Table 2 Amplitude of microsegregation with respect to each alloying element predicted by Scheil simulation at 95% solidification

Alloying elements	Ni	Cu	Cr	Mo	V
Nominal alloy composition—C_{alloy} (at%)	6.38	3.31	2.04	0.36	0.11
Microsegregation amplitude $C_{0.95} - C_0$ (at%)	1.29	1.67	0.72	0.34	0.05

Scheil simulation is a fast method of estimating microsegregation [42]. The main approximations are infinite diffusion in the liquid but no diffusion in the solid phase. This has been coupled to the multicomponent SGTE thermodynamic database using *ThermoCalc*™ from which the solid/liquid equilibrium was calculated repeatedly during the simulation. Figure 18 presents the solidification simulation result as temperature versus fraction solid using the non-equilibrium Scheil simulation and compares it with the full equilibrium case. Figure 19 presents the composition profiles calculated by the Scheil simulation showing the degree of microsegregation in the solid after solidification. Here, the fraction of solid is equivalent to position relative to a dendrite arm center. Previous comparison with more rigorous calculations incorporating solid back diffusion indicate that the Scheil result at 95% solid is a reasonable estimate of the maximum microsegregation amplitude under typical ingot solidification conditions [43]. The results presented in Table 2 predict that Mo has the greatest potential for segregation. However, since the level of Mo in the alloy is relatively low, no serious Mo microsegregation problems are predicted for the designed composition. While the variation of Cu is significant, it was assessed to be acceptable for homogenization treatment at 1,200°C.

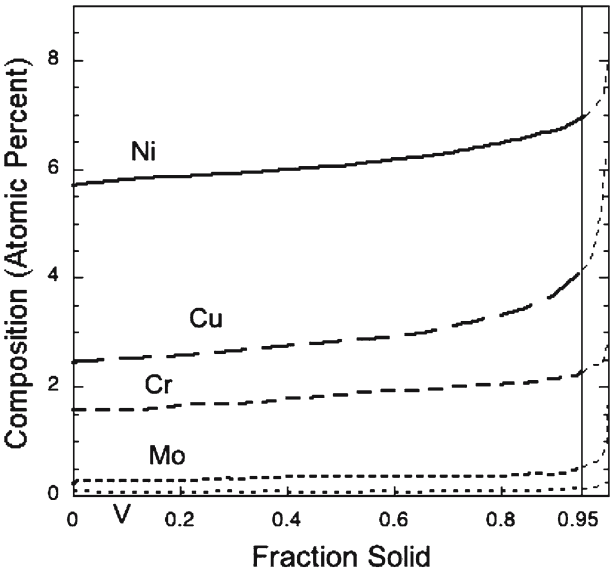

Fig. 19 Scheil simulation for composition profile of each alloying element after solidification for designed alloy Fe–0.05C–6.5Ni–3.65Cu–1.84Cr–0.6Mo–0.1V (wt%). Solid fraction corresponds to position relative to dendrite arm center

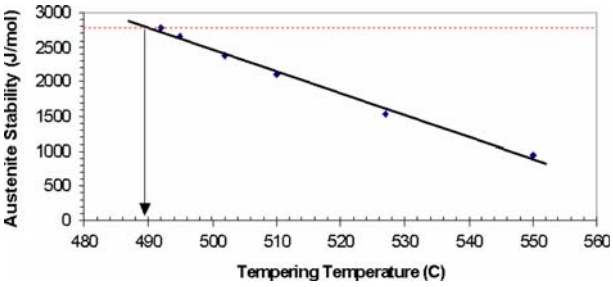

Fig. 20 Room temperature (300 K) stability of austenite as a function of tempering temperature. The required stability is predicted for 490°C

4.3 Selection of tempering temperature

Using multistep tempering to initially nucleate austenite at a high tempering temperature, the austenite stability for this transformation toughened alloy is dependent on the final tempering temperature. With the alloy composition fixed, the austenite stability was then calculated as a function of tempering temperature as shown in Fig. 20. It illustrates that the $\Delta G_{ch} + W_f$ value of 2836 J/mole desired for this alloy is achieved for a tempering temperature of 490°C, very close to the originally assumed temperature of 500°C.

Based on the design calculations, we derive a composition for the ultratough, high strength weldable plate steel (in wt%) with final tempering at 490°C: Fe–0.05C–3.65Cu–6.5Ni–1.84Cr–0.6Mo–0.1V.

The composition should be solution treatable at 900°C, with predicted M_S and B_S transformation temperatures of 298°C and 336°C, respectively. Based on previous transformation toughened steels, it is planned that initial tempering at a slightly elevated temperature will be employed to nucleate the austenite before tempering at 490°C to enrich the Ni content to the designed level. In our judgment, the highest risk assumption of this design is that fine austenite can be heterogeneously nucleated on Cu particles as effectively as it has been observed to nucleate on M_2C carbides [40]. The observed effectiveness of Cu as a nucleant in numerous alloy systems [44,45] supports this assumption.

5 Summary and conclusions

A systematic strategy in computer-aided design of materials has been successfully applied to demonstrate feasibility of an ultratough high-strength weldable plate steel for naval hull applications. The approach integrated processing/structure/property/performance relations with mechanistic models to achieve the desired quantitative property objectives. Quantitative models were used to design the toughening and strengthening dispersions, which were the two major property requirements to be met under stringent processability constraints.

The overall strategy behind the thermodynamic modeling has been to map the mechanical properties objectives to structure and then to thermodynamic parameters to set goals for the design of the microstructural subsystems. The Olson–Cohen model for heterogeneous martensitic nucleation aided the determination of a thermodynamic stability parameter for the austenite. The optimal stability of the transformation-toughened austenite was calibrated against the parameter $(\Delta G_{ch}+W_f)$ combining thermodynamic driving force and interfacial friction to obtain the required toughness, which was the top priority of this design. Then, based on the strength requirement projected to hardness values, the design space was identified. The alloy composition and the processing conditions were subsequently determined by conforming to these parametric design requirements.

The explored design concept is based on the mechanism of dispersed austenite stabilization for transformation toughening adapted to weldable high strength steels. The concept employs mixed bainitic/martensitic microstructures produced by air-cooling of solution-treated plate, combined with copper and alloy carbide precipitation strengthening during secondary tempering, constrained by a low carbon content for weldability. A fine particle dispersion of optimal ~3–5 nm size for effective strengthening was designed by precipitation of M_2C carbides and BCC copper from a highly supersaturated BCC solution. The carbon content of the alloy was set at 0.05 wt% to meet weldability constraints. Based on the carbon level set, a quantitative carbide-strengthening model was used to determine the strength contribution from M_2C carbides, with the driving force for M_2C precipitation maximized at ~14 kJ/mole (while initially maintaining a stoichiometric balance between carbon and the carbide formers Mo, Cr, V) to obtain a fine 3–4 nm precipitate particle size. The additional strengthening required to meet the yield strength goal of 160 ksi (1,100 MPa) was achieved by setting an optimal level of copper at 3.65 wt% based on a quantitative copper-strengthening model. This relatively high Cu level was necessary to allow the low carbon limit. A high Ni/Cu ratio (1.8) was also maintained in the multicomponent alloy design to prevent hot shortness problems during processing.

Transformation toughening arises from dispersed austenite precipitates, which undergo a martensitic transformation at the crack-tip stress state. This leads to inhibition of crack growth by delay of microvoid shear localization during ductile fracture. Thus to achieve high toughening by this mechanism, required stability of the austenite was designed by optimizing Ni as an FCC stabilizer. Thermodynamic calculations predicted an alloy Ni content of 6.5 wt% to enable the equilibrium nickel content of 30% in the austenite to meet the requirement for transformation toughening.

The design also revealed that although Cr did not have a strong effect on the driving force for carbide precipitation, it helped in partitioning Cu out of the austenite phase for effective copper precipitation strengthening; the alloy Cr level was set at 1.8 wt%. The processability conditions were then evaluated under stringent restrictions for the designed alloy (Fe–0.05C–3.65Cu–6.5Ni–1.84Cr–0.6Mo–0.1V; wt%) based on solution treatment condition, microsegregation behavior and tempering condition. A design solution treatment condition of 900°C for 1 h was found sufficient to dissolve M_2C carbides without excessive austenite grain growth. No serious microsegregation problems were predicted for the designed composition based on results from Scheil simulation. A final tempering temperature of 490°C (after a higher temperature austenite nucleation step) was predicted to achieve sufficient austenite stability for transformation toughening. Thus, thermodynamic calculations demonstrated feasibility of combining copper and M_2C carbide precipitation for strengthening in combination with nickel-stabilized austenite for transformation toughening in a relatively low cost weldable plate steel.

Acknowledgements This research was carried out under the financial support by the Office of Naval Research (ONR) under Grant number N00014-01-1-0953 as a part of the ONR Grand Challenge in Naval Materials by Design. The authors are thankful to Dr. Gautam Ghosh (Northwestern University), Dr. C. J. Kuehmann (QuesTek Innovations LLC) and Dr. H. J. Jou (QuesTek Innovations LLC) for their helpful discussions during the alloy design process.

References

1. Olson, G.B.: Computational Design of Hierarchically Structured Materials. Science **277**, 1237–1242 (1997)
2. Olson, G.B.: Pathways of Discovery: Designing a New Material World. Science **288** 993–998 (2000)
3. Gagliano, M.S., Fine, M.E.: Precipitation Kinetics of Niobium Carbide and Copper in a Low Carbon, Chromium-Free Steel. CALPHAD **25**, 207–216 (2001)
4. Haidemenopoulos, G.N., Olson, G.B., Cohen, M.: Dispersed-Phase Transformation Toughening in Ultrahigh-Strength Steels In: Olson, G.B., Azrin, M., Wright, E.S. (eds.) Innovations in Ultrahigh-Strength Steel Technology (34th Sagamore Army Materials Research Conference), pp. 549–593. US Government Printing Office, Washington DC, Lake George, NY (1990)
5. Socrate, S.: Mechanics of Microvoid Nucleation and Growth in High-Strength Metastable Austenitic Steels Doctoral Dissertation, Department of Materials Science and Engineering, Massachusetts Institute of Technology, Cambridge, MA (1995)
6. Olson, G.B., Kuehmann, C.J.: Transformation Toughening in Dispersed Phase Systems In: Austenite Formation and Decomposition Symposium in Mat Sci & Tech 2003 Proc (ISS & TMS), pp. 493–504. Chicago, IL (2003)
7. Ashby, M.F.: Materials Selection in Conceptual Design In: Proc. Ashby Symp. On Materials Design, ASM World Materials Congress, Chicago, IL (1988)
8. Smith, C.S.: A Search for Structure. MIT Press, Cambridge, MA (1981)
9. Jenkins, G.M. The Systems Approach. In: Beishon, J., Peters, G. (eds.) Systems Behavior, pp. 56–79. Open University Press, Birmingham, UK (1972)
10. Stavehaug, F.: Transformation Toughening of γ'-Strengthened Metastable Austenitic Steels Doctoral Dissertation, Department of Materials Science and Engineering, Massachusetts Institute of Technology, Cambridge, MA (1990)

11. Leal, R.H.: Transformation Toughening of Metastable Austenitic Steels. Doctoral Dissertation, Department of Materials Science and Engineering, Massachusetts Institute of Technology, Cambridge, MA (1984)
12. Hsieh, K.C.: Fracture Toughness of Ti-modified Air-melted UHS Steels Doctoral Dissertation Proposal, Department of Materials Science and Engineering, Northwestern University, Evanston, IL (2000)
13. Garrison, W.M., Handerhan, K.J. Fracture Toughness: Particle-Dispersion Correlations In: Olson, G.B., Azrin, M., Wright, E.S. (eds.) Innovations in Ultrahigh-Strength Steel Technology (34th Sagamore Army Materials Research Conference), pp. 443–466. US Government Printing Office, Washington DC, Lake George, NY (1990)
14. Barsom, J.M., Rolfe, S.T.: Fracture and Fatigue Control in Structures: Applications of Fracture Mechanics. Prentice-Hall Inc., Englewood Cliffs, NJ 159–188 (1987)
15. Ritchie, R.O., Francis, B., Server, W.L.: Evaluation of toughness in ALSL 4340 alloy steel austenitized at low and high temperatures Metall. Trans. A **7A**, 831–838 (1976)
16. Ghosh, G., Campbell, C.E., Olson, G.B.: An Analytical Electron Microscopy Study of Paraequilibrium Cementite Precipitation in Ultra-high Strength Steel Metall. Mater. Trans. A **30A**, 501–512 (1999)
17. Wise, J.: Systems Design of Advanced Gear Steels Doctoral Dissertation, Department of Materials Science and Engineering, Northwestern University, Evanston, IL (1998)
18. Geng,W.T., Freeman, A.J., Olson, G.B.: Influence of Alloying Additions on Grain Boundary Cohesion of Transition Metals: First-principles Determination and its Phenomological Extension. Phys. Rev. B **63**, 165415 (2000)
19. Kantner, C.D.: Designing Strength, Toughness and Hydrogen Resistance: Quantum Steel Doctoral Dissertation, Department of Materials Science and Engineering, North-western University, Evanston, IL (2002)
20. Russell, K.C., Brown, L.M.: A Dispersion Strengthening Model Based on Differing Elastic Moduli Applied to the Iron-Copper System Acta Metall. **20**, 969–974 (1972)
21. Foley, R.P., Fine, M.E.: Microstructure and Property Investigation of Quenched and Tempered HSLA-100 Steel In: DeArdo, A.J. (ed.) ISS, Proceedings of the International Conference on Processing, Microstructure and Properties of Microalloyed and Other Modern High Strength Low Alloy Steels, pp. 315–329. Warrendale, PA (1991)
22. Kuehmann, C.J.: Thermal Processing Optimization of Nickel-Cobalt Ultrahigh-Strength Steels Doctoral Dissertation, Department of Materials Science and Engineering, Northwestern University, Evanston, IL (1994)
23. Spaulding, D.: Grain Boundary Cohesion and Segregation in Ultrahigh Strength Alloy Steels Doctoral Dissertation, Department of Materials Science and Engineering, North-western University, Evanston, IL (1995)
24. Ashby, M.F., Jones, D.R.H.: Engineering Materials: An Introduction to their Properties and Application. Pergamon Press, New York (1980)
25. Somers, B.R. Introduction to the Selection of Carbon and Low-Alloy Steels In: ASM Handbook: Welding, Brazing, and Soldering, 6th edn., pp. 405–407. ASM International, Metals Park, Ohio (1993)
26. Gagliano,M.S.: Co-precipitation of Copper and Niobium Carbide in a Low Carbon Steel Doctoral Dissertation, Department of Materials Science and Engineering, North-western University, Evanston, IL (2002)
27. Sundman, B., Jansson, B., Andersson, J.: The Thermo-Calc databank system CALPHAD **9**, 153–190 (1985)
28. Goodman, S.R., Brenner, S.S., Low, J.R.: An FIM-Atom Probe Study of the Precipitation of Copper from Iron-1.4 At. Pct Copper. Part I: Field-Ion Microscopy Metall. Trans. A **4**, 2363–2369 (1973)
29. Goodman, S.R., Brenner, S.S., Low, J.R.: An FIM-Atom Probe Study of the Precipitation of Copper from Iron-1.4 At. Pct Copper. Part II: Atom Probe Analyses Metall. Trans. A **4**, 2371–2378 (1973)
30. Phythian, W.J., Foreman, A.J.E., English, C.A., Buswell, J.T., Hetherington, M., Roberts, K., Pizzini, S.: The Structure and Hardening Mechanism of Copper Precipitation in Thermally Aged or Irradiated Fe-Cu and Fe-Cu-Ni Model Alloys In: Stoller, R.E., Kumar, A.S., Gelles, D.S. (eds.) Effects of Radiation on Materials: 15th International Symposium, pp. 131–150. ASTM STP 1125, Philadelphia, PA (1992)
31. Deschamps, A., Militzer, M., Poole, W.J.: Precipitation Kinetics and Strengthening of a Fe-0.8 wt% Cu alloy ISIJ Int. **41**, 196–205 (2001)

32. Worrall, G.M., Buswell, J.T., English, C.A., Hetherington, M.G., Smith, G.D.W.: A Study of the Precipitation of Copper Particles in a Ferrite Matrix J. Nucl. Mater. **148**, 107–114 (1987)
33. Hornbogen, E. In: Speich, G.R., Clark J.B. (eds.) Precipitation from Iron-Base Alloys. Gordon and Breach, New York, NY (1965)
34. Pizzini, S., Roberts, K.J., Phythian, W.J., English, C.A., Greaves, G.N.: A Fluorescence EXAFS Study of the Structure of Copper-rich precipitates in Fe-Cu and Fe-Cu-Ni Alloys Phil. Mag. Lett. **61**, 223–229 (1990)
35. Phythian, W.J., Dumbill, S., Brown, P., Sinclair, R.: Stability of Thermally Induced Copper Precipitates Under Neutron Irradiation In: Proceedings of the 6th International Symposium on Environmental Degradation in Nuclear Power Systems –Water reactors, pp. 729-737. TMS (1993)
36. Gore, M.J., Olson, G.B., Cohen, M.: Grain-Refining Dispersions and Properties in Ultrahigh Strength Steels In: Olson, G.B., Azrin, M., Wright, E.S. (eds.) Innovations in Ultrahigh-Strength Steel Technology (34th Sagamore Army Materials Research Conference), pp. 425–441. US Government Printing Office, Washington DC, Lake George, NY (1990)
37. Olson, G.B., Tsuzaki, K., Cohen, M.: Statistical Aspects of Martensitic nucleation. In: Cargill, G.S., Spaepen, F., Tu, K.N. (eds.) David Turnbull Symposium on Phase Transitions in Condensed Systems, vol. 57, pp. 127–148. MRS, Pittsburgh, PA (1987)
38. Ghosh, G., Olson, G.B.: Kinetics of FCCBCC Heterogeneous Martensitic Nucleation – I. The Critical Driving Force for Athermal Nucleation Acta Mater. **42**, 3361–3370 (1994)
39. Ghosh, G., Olson, G.B.: Kinetics of FCCBCC Heterogeneous Martensitic Nucleation – II. Thermal Activation Acta Mater. **42**, 3371–3379 (1994)
40. Lippard, H.E.: Microanalytical Investigations of Transformation Toughened Co–Ni Steels Doctoral Dissertation, Department of Materials Science and Engineering, North-western University, Evanston, IL (1999)
41. Campbell, C.E., Olson, G.B.: Systems design of high performance stainless steels I. Conceptual and computational design J. Comput. Aided Mat. Design **7**, 145–170 (2000)
42. Scheil, E.: "Bemerkungen zur Schichtkristallbildung Z. Metallkd. **34**, 70–72 (1942)
43. Lippard, H.E., Campbell, C.E., Bjorklind, T., Borggren, U., Kellgren, P., Dravid, V.P., Olson, G.B.: Microsegregation behavior during solidification and homogenization of AerMet100 steel Metall. Mater. Trans. B **29**, 205–210 (1998)
44. Hono, K., Ping, D.H., Ohnuma, M., Onodera, O.: Cu Clustering and Si Partitioning in the Early Crystallization Stage of an $Fe_{73.5}Si_{13.5}B_9Nb_3Cu_1$ Amorphous Alloy Acta Mater. **47**, 997–1006 (1999)
45. Ohkubo, T., Kai, H., Ping, D.H., Hono, K., Hirotsu, Y.: Mechanism of Heterogeneous Nucleation of α-Fe Nanocrystals from $Fe_{89}Zr_7B_3Cu_1$ Amorphous Alloy Scripta Mater. **44**, 971–976 (2001)